Total-Internal-Reflection-Fluorescence Microscopy for the Study of Nanobubble Dynamics

Chon U Chan and Claus-Dieter Ohl

Division of Physics and Applied Physics, School of Physical and Mathematical Sciences, Nanyang Technological University,
Singapore 637371, Singapore
(Received 12 April 2012; published 23 October 2012)

Nanobubbles can be observed with optical microscopy using the total-internal-reflection-fluorescence excitation. We report on total-internal-reflection-fluorescence visualization using rhodamine 6G at 5 μM concentration which results in strongly contrasting pictures. The preferential absorption and the high spatial resolution allow us to detect nanobubbles with diameters of 230 nm and above. We resolve the nucleation dynamics during the water-ethanol-water exchange: within 4 min after exchange the bubbles nucleate and form a stable population. Additionally, we demonstrate that tracer particles near to the nanobubbles are following Brownian motion: the remaining drift flow is weaker than a few micrometers per second at a distance of 400 nm from the nanobubble's center.

Introduction.—Nanobubbles are nanometer high gas bodies attached to a surface being immersed in a liquid [1]. In particular, the study of surface stabilized nanobubbles in water has attracted a lot of attention because of their potential role for interfacial water technologies [2,3]. So far nanobubbles mostly have been studied with scanning atomic force microscopy (AFM) which offers a very high spatial resolution (below 1 nm). The downside is the long scanning time which prevents a study of their short time dynamics. Higher temporal resolution has been achieved with single line scans of the AFM tip [4] or with IR spectroscopy, e.g., Refs. [5,6].

In this Letter, we report on the visualization of stabilized nanobubbles on a *hydrophilic* surface with a standard optical microscopy technique. A common procedure to create surface nanobubbles on hydrophilic interfaces is the water-ethanol-water exchange process. There, the water is replaced first by ethanol and then by water [7]. The higher solubility of gas in ethanol and the exothermic mixing of ethanol with water leads to the release of dissolved gas from the ethanol. The subsequent replacement of the ethanol with the now supersaturated water is responsible for the nucleation of nanobubbles, see Ref. [8] and further studies summarized in Ref. [1]. The recent review by Seddon and Lohse [1] pointed out that for success in understanding the physics of nanobubbles, the experimental reproducibility has to be improved, the nucleation process detailed, and indications on a possible dynamic equilibrium collected. All these questions demand for an experimental technique which not only can resolve the surface nanobubbles but also study their dynamics with a much better temporal resolution than is currently available. In this Letter, we present an experimental technique which can help to solve some of the remaining puzzles in nanobubble research.

We first describe the experimental technique to visualize surface nanobubbles and then discuss the dynamics of

bubble formation during the water-ethanol-water exchange using this optical technique. The physical principle behind optical nanobubble detection is total-internal-reflection-fluorescence (TIRF) microscopy. TIRF allows us to illuminate only a very thin volume of liquid in contact with an interface, i.e., between glass and water. For our geometry, the total-internal-reflection occurs for an angle $\theta_{tot} > \sin^{-1}(n_w/n_g) \approx 61°$, where $n_w = 1.33$ and $n_g = 1.52$ are the indexes of refraction for water and the microscope cover glass, respectively. In the experiment, we can achieve conveniently this angle of incidence; the maximum possible angle θ has been determined with a prism and is about 74°. The corresponding penetration depth (that is where the intensity drops to $1/e$) can be estimated [9] as 70 nm by $z_0 = \lambda(4\pi\sqrt{(n_g \sin\theta)^2 - n_w^2})^{-1}$, where λ is the laser wavelength.

Experimental setup.—Figure 1(a) depicts the beam formation and injection into the microscope. We use a green solid state cw laser (40 μW, $\lambda = 532$ nm) expanded to 12 mm in diameter and steered into the side port of an inverted microscope (Olympus IX71). A mirror and a lens set the angle of incidence θ, the mirror ($M1$) steers and the lens ($L3$) focuses the beam into the back focal aperture of the microscope objective (Olympus ApoN 60x, NA 1.49). By adjusting the rotating mirror $M1$ located at the back focal plane of $L3$, the incident angle θ can be varied while the illumination spot remains fixed and within the field of view. Due to the limited working distance of the high-NA microscope objective, only thin glass plates (here, a cover slip glass no. 1 with 140 μm thickness) can be used. A cooled slow scan CCD camera (Sensicam QE, PCO, Germany) with a pixel size of 6.45×6.45 μm^2 is used for imaging. We have measured a pixel resolution of 108 nm/pixel. The diffraction limited resolution for the objective is about 230 nm (at 550 nm). The camera records a field of view of 55×69 μm^2 with a typical exposure
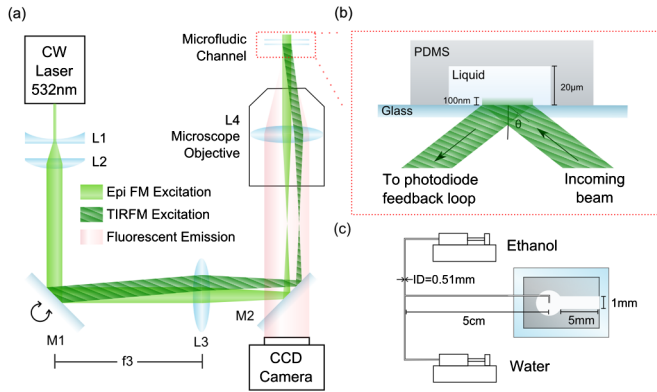
FIG. 1 (color online). (a) Sketch of the optical path for TIRF microscopy. Epifluorescence and TIRF microscopy excitations are available by rotating mirror $M1$. (b) Cross section of the polydimethylsiloxane channel to study the water-ethanol-water exchange. (c) Schematic of the flow line consisting of two syringes and syringe pumps, a T connection, and a 5 cm feed to the microchannel. The microchannel is 5 mm long and 1 mm wide.

time of 25–40 ms at 18 frames/s. This is sufficiently fast to resolve the nanobubble nucleation dynamics (see below).

Figure 1(b) sketches the side view of the beam reflecting from the glass-liquid interface. The liquid is transported in a microchannel with a rectangular cross section (1 mm width, 20 μm height). The channel is fabricated with standard soft lithography technique, the patterned polydimethylsiloxane channel bonded on a glass cover slip (Menzel-Glaser, Germany) precleaned in an ultrasonic bath. 5 μM rhodamine 6G fluorescent dye is dissolved both in the deionized water (purification with Sartorius Arium 611vf, France) and in 99% ethanol (Riverbank Chemicals, Singapore). Both liquids are loaded into separate syringes. They are discharged in sequence using syringe pumps. Before the liquids reach the channel, they flow through a T junction which is about 5 cm away from the channel inlet. When the flow channel is operated, some pressure builds up which eventually flexes the cover slip glass mildly. Therefore, the distance of the microscope objective has to be adjusted during the experiment. The manual height adjustment is aided by a back reflection of the laser beam. This reflection passes over an aperture and is detected with a photodiode [not shown in Fig. 1(a)]. During the experiments, the photodiode signal is kept constant by adjusting the stage manually and thus, keeping the distance between the objective and glass constant.

Nucleation dynamics during water ethanol exchange.— Figure 2(a) demonstrates a typical figure recorded after the water-ethanol-water exchange in TIRF mode. The surface lights up with disc shaped objects filling almost completely the surface of the glass cover slip. Before the exchange, an unstructured dim light is recorded. Yet, after the exchange protocol, strong contrasted objects appear. We attribute these objects to surface nanobubbles. The typical contrast
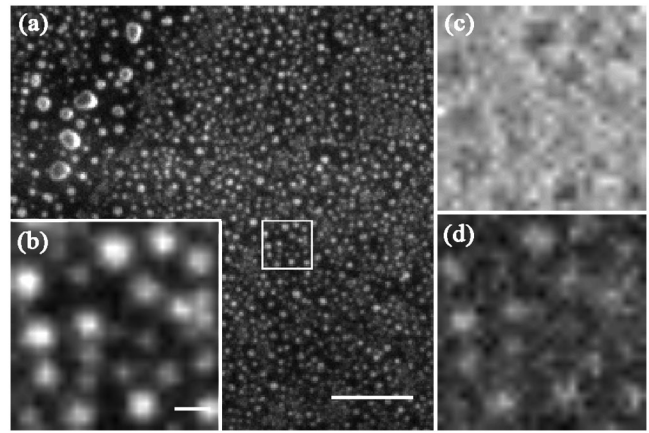

FIG. 2. (a) Nanobubbles observed under TIRF microscopy. Scale bar is 5 μm. The square area is zoomed into for comparison of the different technique (b) TIRF microscopy (scale bar is 500 nm), (c) brightfield, and (d) epifluorescence.

of the surface bubbles as defined by $(I_{\max} - I_{\min})/(I_{\max} + I_{\min})$ is approximately 0.5 and the signal to noise ratio is 3.

Figures 2(b)–2(d) are enlarged views of the area indicated with a white square in Fig. 2(a) (scale bar length is 500 nm). For magnification, they are resampled using linear splines. Figure 2(b) is just the enlarged part of Fig. 2(a), while Figs. 2(c) and 2(d) compare the same view in brightfield mode and in epifluorescence ($\theta = 0°$), respectively. From this comparison, it becomes clear that the TIRF microscopy provides a strong contrast for nanobubble visualization. Nanobubbles are not visible in the brightfield mode, and only some of the largest structures weakly appear in the epifluorescence mode.

What leads to the stark contrast of nanobubbles under TIR illumination? It is well-known that rhodamine is accumulating at liquid-gas interfaces. Zheng *et al.* [10] demonstrate that the fluorescence is about 60 times stronger from the water-air interfaces as compared to the bulk. Thus, we explain the strong contrast of nanobubbles in TIRF microscopy by the combination of adsorption of rhodamine at the nanobubble interface and the short penetration depth of the evanescent wave exciting preferentially the liquid on the scale of the nanobubble height, i.e., about 100 nm.

Although the water-ethanol-water exchange is a common method to generate nanobubbles on hydrophilic surfaces, very few measurements on the nucleation dynamics are available. The microbalance techniques predicts that the nanobubbles are formed within one minute after the liquid exchange [11].

Figure 3 presents the different stages leading to a surface decorated with nanobubbles. For this experiment, both syringes holding water and ethanol are discharged one after another. Initially, the feed line and the whole microchannel is filled with water, see Fig. 1(c). Then, a fast flow (Ethanol) of 125 μl/min transports the water-ethanol
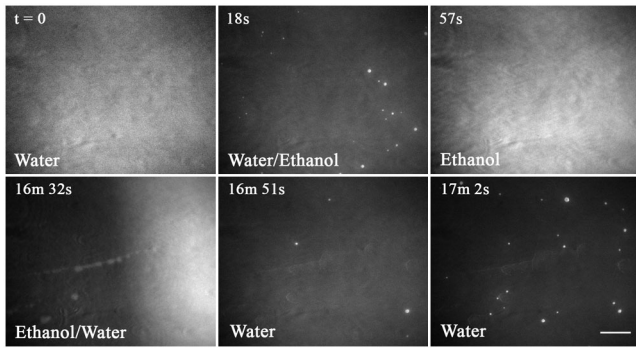
FIG. 3. Snapshots of images obtained during water-ethanol-water exchange. The intensity is normalized for each frame. Upper row: bubbles are formed when water is replaced by ethanol. These bubbles dissolved quickly. Lower row: bubbles again nucleate when ethanol is replaced by water. Bubbles continue to nucleate after the exchange is finished. Scale bar is 10 μm.

interface from the T junction to the inlet of the microchannel. Thereby, we reduce diffusion at the T junction liquid-liquid interface. Then, a slow flow of 1 μl/min pushes the interface through the microchannel. The dynamics are presented in Fig. 3: at time $t = 0$, the channel is filled with water only. At time $t = 18$ s, the water is partly replaced from the left with ethanol and quickly bright spots appear on the surface. These nanobubbles, however, quickly dissolve and after 40 s, all bubbles have dissolved. Then, we keep ethanol for about 15 minutes in the channel before starting the replacement. Again, for this exchange, the water is pushed initially with a fast flow through the feed line followed by a slow flow through the microchannel. At $t = 16$ min 32 s, the water front arrives at the field of view and pushes out the ethanol to the right. At time $t = 16$ min 51 s, the microchannel is completely filled with water and the nanobubbles start to nucleate. Eleven seconds later, many more nanonbubbles have nucleated, see last frame of Fig. 3.

Experiments not detailed here revealed that the flow rate affects the nucleation speed. At higher flow rates (about 50 μl/min), nucleation completes almost instantly once the liquid-liquid interface has passed. While at smaller flow rates, e.g., 5 μl/min and below, nucleation may take several minutes before a steady nanobubble population is reached. The temporal development of nanobubble nucleation at a flow rate of 5 μl/min is shown in Fig. 4. At time $t = 2.5$ min after water-ethanol-water exchange, a few isolated nanobubbles appear. Two minutes later, the surface shows about 0.1 bubbles/μm^2; another 2 minutes, the surface density has quadrupled. Figure 5 plots the nanobubble density as a function of time. The rise time of the nanobubble density, i.e., from 10 to 90% of the maximum bubble density, is about 240 s. An analysis of the nanobubble diameter is presented in Fig. 5. We understand that bubbles below the resolution limit of about
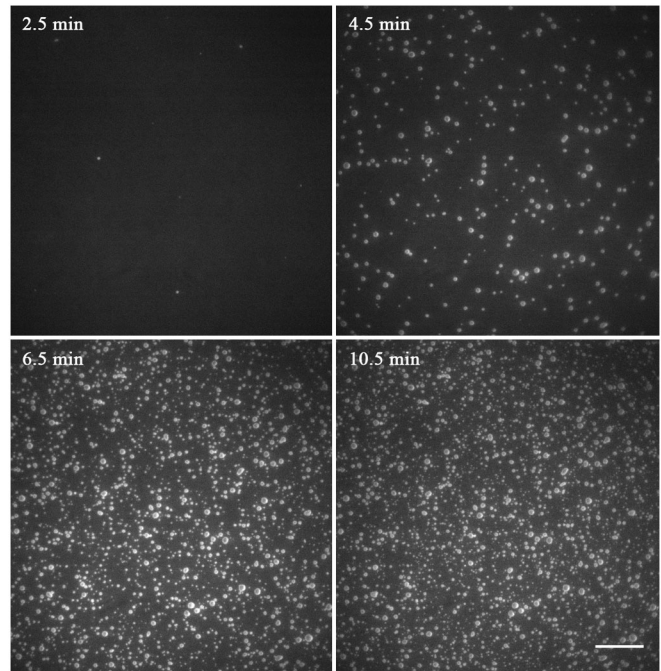

FIG. 4. The channel is filled with water after water-ethanol-water exchange. Bubbles nucleate gradually over several minutes. The exchange flow is from left to right. The scale bar is 10 μm.

230 nm can't be resolved. Thus, the distribution only shows relatively large diameter nanobubbles. Similar sizes with diameters of up to 1 μm have been observed on rough surfaces [12].

Residual flow close to nanobubbles.—The optical detection of nanobubbles allows us to combine the technique with other microscope-based observation techniques.
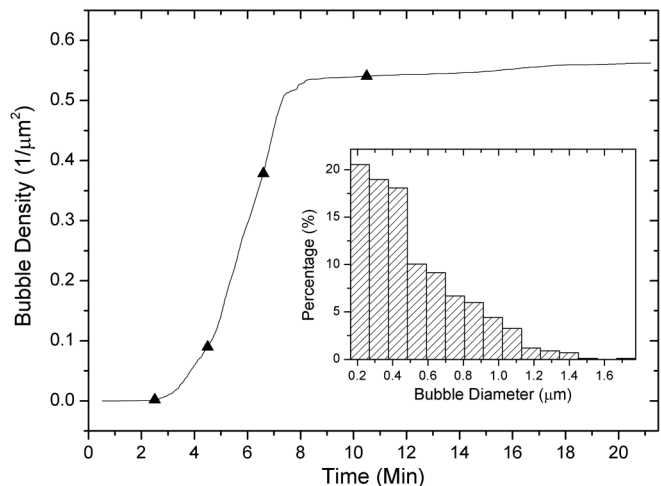

FIG. 5. The bubble density plotted as a function of time for the experiment shown in Fig. 4. The triangles state the times where the snapshots in Fig. 4 are taken. Inset figure provides size distribution of the bubbles formed. Bins increase by the pixel size. The smallest bin is 2 pixels wide.
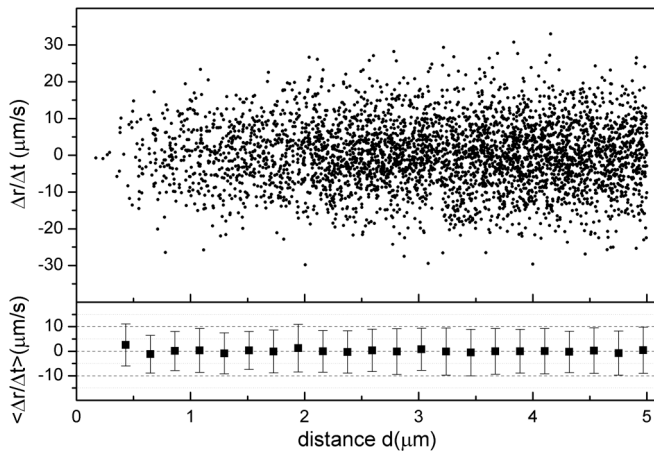
FIG. 6.   Upper: differential speed of the particle as a function of distance to nanobubble center. Lower: mean value of differential speed at each distance interval. The first interval centered at 0.43 μm. Each interval width is 0.11 μm.

Using small tracer particles, we can probe if the Brownian motion of particles is affected near to the nanobubbles. It has been proposed that nanobubbles are stabilized against dissolution through a recirculating flow emanating from the apex of the bubble towards its three-phase contact line [13]. Their AFM measurements agree with a model utilizing a Knudsen gas leading to a jetting flow of several meters per second and starting at the nanobubble's apex. This jetting flow should then drive a bulk recirculating flow with a lateral dimension of at least the lateral size of the nanobubble. We are probing this flow by tracking the motion of 200 nm diameter red fluorescent particles near to and far from the nanobubbles. Areas on the surface with a low density of nanobubbles are first chosen. Then, the locations of the nanobubbles are identified. We photo bleach the nanobubbles by increasing the laser power to 150 mW to increase the contrast of the particles near to them and then slowly replace the water with deionized water containing the nanoparticles. The particles are recorded at 21 frames/s ($\Delta t \approx 48$ ms) with an exposure time of 1 ms and the tracks are obtained from image processing [14]. We then analyze the differential speed of the particle $\Delta r / \Delta t (d) = \pm |[\mathbf{r}(t + \Delta t) - \mathbf{r}(t)]| / \Delta t$ as a function of the distance $d = |[\mathbf{r}(t + \Delta t) + \mathbf{r}(t)]|/2$, where $\mathbf{r}(t)$ is the distance vector to nanobubble center in each frame. The recirculating flow would lead to a preferential particle motion close to the surface towards the three-phase contact line. Our spatial resolution of approximately 100 nm is able to detect drift velocities larger than 2 μm/s, which is about 6 orders of magnitude smaller than the predicted jet velocity. We have analyzed 18 nanobubbles with altogether 2000 tracks. Figure 6 analyzes the result from the particle tracking: we measure particle speeds of up to 30 μm/s independent of the distance. The averaged velocity is very close to zero; it is less than $+2$ μm/s for all measured distances. A study of the mean-square-displacement [14] demonstrates that the particles follow Brownian motion. We find no indication of a recirculating flow close to the nanobubble.

In summary.—We have presented the formation of nanobubbles on a hydrophilic glass surface during the water-ethanol-water exchange in a microchannel. The growth dynamic has been captured optically with a TIRF microscope. We achieved a temporal resolution with a cooled CCD camera and a low power green laser of 56 ms. The pixel resolution of our setup allows us to observe nanobubbles with diameters of 230 nm and above. Additionally, we demonstrate that the motion of nanoparticles close to nanobubbles is dominated by Brownian motion. Even at a distance of 430 nm from the nanobubble center, we find no drift velocity larger than the resolution limit of 2 μm/s.

The TIRF based technique may help to address many more open questions on interfacial nanobubbles. A nonexhaustive list is the superstability to strong tension waves [15], their acoustic resonance [16], and their ability to reduce viscous drag [3,17] in nanochannels.

[1] J. R. T. Seddon and D. Lohse, J. Phys. Condens. Matter **23**, 133 001 (2011).
[2] G. Liu and V. S. J. Craig, ACS Appl. Mater. Interfaces **1**, 481 (2009).
[3] Y. Wang and B. Bhushan, Soft Matter **6**, 29 (2010).
[4] S. Yang, P. Tsai, E. S. Kooij, A. Prosperetti, H. J. W. Zandvliet, and D. Lohse, Langmuir **25**, 1466 (2009).
[5] X. H. Zhang, A. Khan, and W. A. Ducker, Phys. Rev. Lett. **98**, 136101 (2007).
[6] X. H. Zhang, A. Quinn, and W. A. Ducker, Langmuir **24**, 4756 (2008).
[7] S. Lou, J. Gao, X. Xiao, X. Li, G. Li, Y. Zhang, M. Li, J. Sun, X. Li, and J. Hu, Mater. Charact. **48**, 211 (2002).
[8] S. Lou, Z. Ouyang, Y. Zhang, X. Li, J. Hu, M. Li, and F. Yang, J. Vac. Sci. Technol. B **18**, 2573 (2000).
[9] D. Axelrod, T. P. Burghardt, and N. L. Thompson, Annu. Rev. Biophys. **13**, 247 (1984).
[10] X. H. Zhang, A. Harata, and T. Ogawa, Spectrochim. Acta, Part A **57**, 315 (2001).
[11] X. H. Zhang, Phys. Chem. Chem. Phys. **10**, 6842 (2008).
[12] B. M. Borkent, S. de Beer, F. Mugele, and D. Lohse, Langmuir **26**, 260 (2010).
[13] J. R. T. Seddon, H. J. W. Zandvliet, and D. Lohse, Phys. Rev. Lett. **107**, 116101 (2011).

[14] See Supplemental Material at http://link.aps.org/
supplemental/10.1103/PhysRevLett.109.174501 for de-
tails of estimation of nanobubble density, particle tracking,
and validation of the Brownian motion.

[15] B. M. Borkent, S. M. Dammer, H. Schonherr,
G. J. Vancso, and D. Lohse, Phys. Rev. Lett. **98**, 204502
(2007).

[16] H. Rathgen, K. Sugiyama, C. D. Ohl, D. Lohse, and
F. Mugele, Phys. Rev. Lett. **99**, 214501 (2007).

[17] A. Steinberger, C. Cottin-Bizonne, P. Kleimann, and
E. Charlaix, Nature Mater. **6**, 665 (2007).

[18] S. Karpitschka, E. Dietrich, J. R. T. Seddon, H. J. W.
Zandvliet, D. Lohse, and H. Riegler, Phys. Rev. Lett.
109, 066102 (2012).